# 3

# Time Domain Optical Imaging of Ferromagnetodynamics

B.C. Choi and M.R. Freeman

Understanding the magnetic properties of small magnetic elements has become a major challenge in fundamental physics, involving both static and dynamic properties. The importance to technological applications such as high-density magnetic storage is also clear. The investigation of such small magnetic structures relies increasingly on magnetic imaging techniques, since the relevant properties can vary over length scales from micrometers to nanometers. This chapter describes an experimental method for measuring the fast magnetic phenomena in lithographically fabricated magnetic elements in the picosecond temporal regime and with sub-micrometer spatial resolution. The method employs stroboscopic scanning microscopy and is capable of measuring simultaneously all three components of the magnetization vector. This technique allows direct insight into the spatiotemporal evolution of dynamic processes, including ferromagnetic resonance and magnetization reversal in small magnetic elements.

## 3.1 Introduction

Magnetic phenomena on short time scales are different in many aspects from the static case [1, 2]. Moreover, the fast magnetic phenomena in small patterned elements have little relation to that in continuous films, due to the magnetostatics of element edges, which modify the equilibrium states of the elements in terms of the magnetic moment distribution [3–5]. From an application point of view, it has become crucial to understand reversal dynamics on fast (in the nano- and picosecond range) time scales in magnetic elements with dimensions in the micrometer size regime and below. This is owing to the increasing demands on conventional storage technologies and for newer approaches such as magnetic random access memories (MRAM) [6, 7]. Motivated by all of these accumulated interests, magnetization dynamics in micro- and nano-sized magnets are being actively studied by a number of groups [8–15].

In order to elucidate magnetization dynamics, direct observations of the magnetization configuration during reversal processes are most desirable. Imaging of micromagnetic domain structures has been carried out, for example, by magnetic force microscopy (MFM) [16], Lorentz transmission electron microscopy [17] and

scanning electron microscope with polarization analysis (SEMPA) [18, 19], in addition to magneto-optic microscopy [3]. These techniques provide a good spatial resolution, but are generally focused on quasi-static magnetic imaging. For the study of magnetization dynamics, it has been demonstrated that very high spatiotemporal resolution can be achieved by employing stroboscopic scanning Kerr microscopy with pulse excitation [20–23]. This technique is a powerful tool for dynamic micromagnetic imaging and is the topic of this chapter.

### 3.1.1 Historical Background of Time-Resolved Techniques

The development of proper tools to study fast magnetic phenomena has a long history. In this research field, there have been two widely used experimental techniques; i.e., inductive and imaging methods. The former is to infer the magnetic flux changes by measuring the induced voltage in loops around the sample, whereas the latter is to observe the magnetization configuration using the magneto-optic Kerr effect. Kerr microscopy gives a more detailed picture of the magnetization configuration than does the use of pickup loops. The imaging technique, however, has not been extensively used for dynamics studies due to the complex instrumental requirements. A brief description of the development of these two competitive techniques is given below.

In the early 1960s, Dietrich and his coworkers measured magnetization switching speeds of 1 ns in Permalloy ($Ni_{80}Fe_{20}$) films using an inductive technique [24]. This approach used the discharge of a 50 V charge line through a coaxial mercury relay as a pulsed current and, therefore, pulsed magnetic field source. Strip transmission lines were used to deliver the magnetic pulse to the sample, and pickup coils were positioned around the transmission lines to detect the inductive signal from the changing magnetization in the sample. In their fast-switching experiments, free oscillations in the inductive signal, indicative of underdamped magnetic precession, were observed when magnetic pulses were applied transverse to the easy axis of the film. Since Dietrich's experiment, the inductive technique has been improved in many ways [25, 26]; a time-domain transmission geometry is used in order to avoid the need for inductive pickup coils, lithographically patterned coplanar waveguides are used to deliver magnetic pulses to the samples, modern pulse sources are used to create much faster pulses than can be obtained from mercury reed relays, and digital signal processing is employed to improve signal-to-noise ratios. With such improvements in the performance, impulse- and step-response experiments were recently carried out on a 50-nm-thick $Ni_{80}Fe_{20}$ element (1 mm $\times$ 50 $\mu$m) to infer that free magnetization oscillations occurred with rotation times as short as 200 ps [26].

Contemporary inductive and related electronic approaches exploit magnetic thin film devices for characterizing the high-speed dynamics [15, 27]. Koch et al. [15] probed the magnetization dynamics in thin film elements using spin-dependent tunnel junctions, in which a change in the tunneling resistance between two magnetic layers, i.e., a pinned (Co) and a free ($Ni_{60}Fe_{40}$) magnetic layer separated by an $Al_2O_3$ tunnel junction, was measured. Using this technique, the time required to reverse the magnetization direction of the soft ferromagnetic $Ni_{60}Fe_{40}$ layer is measured from greater than 10 ns to less than 500 ps as the amplitude of the applied magnetic field

pulse is increased up to 8 kA/m. The optically induced modulation experiment is also of interest, which is carried out in exchange biased ferromagnetic/antiferromagnetic (FM/AF) bilayer ($Ni_{81}Fe_{19}$/NiO) structures [22]. In this experiment, large modulation in the unidirectional exchange bias field is induced via photoexcitation of the FM/AF interface with sub-picosecond laser pulses. Consequently, the unpinning of the exchange bias leads to coherent magnetization rotation in the permalloy film on a time scale of 100 psec.

While the inductive techniques described above are being actively pursued, all of these methods suffer from drawbacks that are not shared by the time-resolved imaging technique capable of giving a picture of the magnetization configuration during a magnetization reversal. The first high bandwidth spatially resolved optical experiments also date back to the 1960s, when J.F. Dillon and coworkers "saw" ferromagnetic resonance in a sample of 45-μm-thick $CrBr_3$ using microwave optical technique [28]. In the late 1960s, Kryder et al. first presented spatially and temporally resolved dynamic magnetization configuration in magnetic thin films with "a nanosecond Kerr magneto-optic camera" [29]. This Kerr photo-apparatus enabled one to capture magnetization reversal process in $Ni_{83}Fe_{17}$ films with a 10 μm spatial resolution and a 10 ns temporal resolution. This spatiotemporal resolution was an enormous achievement even by today's standard.

The time-resolved imaging technique, however, has not been used extensively at higher speeds because the instrumentation required is very complex. Revival of interest in fast imaging techniques began to take place in the mid-1980s. Kasiraj et al. reported magnetic domain imaging with a scanning Kerr effect microscope [30], in which a digital imaging technique was used with a spatial resolution of less than 0.5 μm. This allowed the observation of the nucleation and growth of magnetic domains in the pole tip region of a recording head. In this implementation, a time resolution of 50 ns was achieved. Subsequently, ultrafast (in the picosecond range) optical technique was developed by Freeman in 1991 [31]. In this work picosecond-scale magnetic field pulses were launched from a photoconductive switch and applied to samples, which were then probed by time-delayed optical pulses, yielding temporal information in a conventional stroboscopic manner. This pioneering work extended so-called "pump-and-probe" technique to the field of magnetics, providing an experimental tool for the study of picosecond time-resolved magnetization reversal dynamics. Since then, a number of spatiotemporally resolved experiments to directly measure the dynamical evolution of magnetization configuration have been reported, in particular, in microstructured elements [13, 20, 23, 32, 33]. During recent years, a similar experimental method has been used by several groups like Acremann et al. [14] and Hicken et al. [34].

Recently, spatiotemporal magneto-optic imaging technique was combined with second-harmonic magneto-optic Kerr effect (SHMOKE), whereby a magnetic sample is illuminated with light at frequency $f$ and generates light at $2f$ [21]. This new method is a good complement to linear magneto-optics, since SHMOKE offers a unique feature that shows an extreme sensitivity to the magnetization at surfaces and interfaces [35]. The temporal images, however, do not provide a good spatial resolution yet, due to the low second-harmonic ($2f$) signal [36].

A further prospect in the field of magnetization dynamics is a time-resolved technique based on X-ray magnetic circular dichroism (XMCD) [37, Chap. 1 and 2 of this book]. This technique provides element selectivity, which is obtained as the X-ray energy is tuned to the adsorption edge of the desired element and is useful for studying separately each magnetic layer in multilayers like a spin valve system. Recent efforts to use pulsed X-ray beam from synchrotron radiation for the study of time-resolved and element-selective magnetization dynamics have been fruitful [38, 39].

## 3.2 Instrumentation

This section introduces the magneto-optic Kerr effect and time-resolved magnetic imaging technique for measuring high-speed magnetic phenomena. Such measurements on very short time scales (e.g., picosecond regime) involve many techniques such as the generation of fast magnetic pulses, precise control of time intervals between the pump and probe beam, and detection of magnetic signals by means of high frequency techniques.

### 3.2.1 Physical Principle of Magneto-Optic Effect

A simple way to dynamically probe the magnetization is by means of interactions of light with a magnetic medium. When linearly polarized light is reflected from a magnetic surface, the incident light is transformed into elliptically polarized light [3]. Thus, the final state of polarization can be characterized by both a rotation of the major axis $\theta_K$ and an ellipticity $\delta_K$ defined as the ratio between the minor and major axes. Both $\theta_K$ and $\delta_K$ are proportional to the magnetization of the material (however, not to the applied magnetic field). This effect is known as the magneto-optic Kerr effect (MOKE) [40]. If light transmission through the magnetic film is considered instead of reflection, then it is termed the Faraday effect. Faraday rotations of $\sim 10^{-3}$–$10^{-2}$ degrees/Å are reported for iron, while the Kerr rotation is on the order of $\sim 10^{-4}$–$10^{-3}$ degrees per monolayer [41].

Microscopically, it is known that the magneto-optic effect originates from the coupling of the electric field of the light and the magnetization of the spin system occurring through the light-induced electronic dipole transitions associated with spin-orbit interaction [42]. Macroscopically, the magneto-optic effect can be described by the inequivalent interaction of polarized light with the magnetization of the material by the two oppositely handed circularly polarized components of the incident light, since the right and left circularly polarized light propagates in the magnetic material with different velocities $v_\pm = c/N_\pm$. The signs $+$ and $-$ refer to the right and left circularly polarized light, respectively. $N_\pm$ are the complex refractive indices and are written as $N_\pm = n_\pm - \mathrm{i}k_\pm$, where $n_\pm$ are refractive indices and $k_\pm$ the extinction coefficients that are related to the optical absorption. For cubic materials where the incidence angle of light and the direction of the magnetization are arbitrary, the complex refractive index is related to the dielectric tensor $\overline{\overline{\varepsilon}}$ as follows [40]:

$$\overline{\overline{\varepsilon}} = N^2 \begin{pmatrix} 1 & iQm_3 & -iQm_2 \\ -iQm_3 & 1 & iQm_1 \\ iQm_2 & -iQm_1 & 1 \end{pmatrix}, \tag{3.1}$$

where $\boldsymbol{m}$ is the magnetization unit vector and $Q$ the material-specific magneto-optic constant, which is proportional to the magnetization. From the equation (3.1) above, it is clearly seen that the off-diagonal terms in the dielectric tensor $\overline{\overline{\varepsilon}}$ represent the magneto-optic effect contribution to $\varepsilon$ and that these terms vanish in the absence of the magnetization.

The interaction of the electromagnetic field with the magnetic material can also be described phenomenologically by the Lorentz force, which gives rise to a change in polarization. This relation is deduced from the dielectric tensor in the equation (3.1), which can be expressed as follows:

$$\boldsymbol{D} = \varepsilon \boldsymbol{E} + \mathrm{i}\varepsilon Q \boldsymbol{m} \times \boldsymbol{E}\,. \tag{3.2}$$

As shown in this equation, the origin of the magneto-optical effect can be represented by the magnetization vector $\boldsymbol{m}$ and the electric field vector $\boldsymbol{E}$ of light. This relation is illustrated in Fig. 3.1, in which a longitudinal Kerr effect measurement is represented. If the linearly polarized light with electric field amplitude $E$ is incident, the electric field induces the oscillation of electrons in its direction. Therefore, without the magneto-optic effect, the reflected light $\boldsymbol{E}_r$ is also linearly polarized parallel to the incident electric field vector $\boldsymbol{E}_i$. If it is supposed that the material is magnetized, then the oscillating electrons will feel the additional Lorentz force $\nu_{\mathrm{Lor}}$, which induces a small motion perpendicular to $\boldsymbol{m}$. Thus, the reflected light contains a small perpendicular component in the electric field vector $\boldsymbol{E}_k$ compared with the incident field vector $\boldsymbol{E}_i$. This component contributes to the magneto-optic Kerr amplitude.

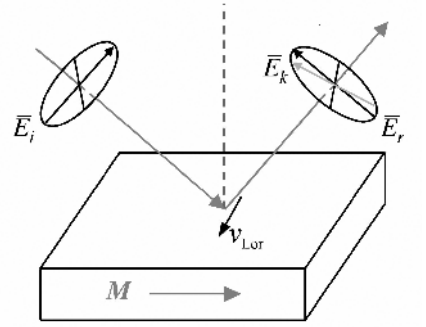


**Fig. 3.1.** Phenomenological description of magneto-optic Kerr effect by means of Lorentz force $\nu_{\mathrm{Lor}}$. Illustrated is the longitudinal Kerr configuration, i.e., the magnetization orientation lies in the incident plane

### 3.2.2 Time-Resolved Experiments

Time-resolved experiments directly measure the dynamic evolution of systems, away from or toward equilibrium, in response to sudden perturbations. For such measurements, a so-called "pump-and-probe" technique is widely used [43]. The method is schematically illustrated in Fig. 3.2. The experimental implementation of time-resolved methods relies, for example, on ultrashort optical pulses. One part of the pulses is used to excite a nonequilibrium state in the system, $\varphi$, at the time $t = t_0$ ("pumping"), while the delayed part of light pulses is used to detect the corresponding change in the system at $t = t_0 + \Delta t$ ("probing"). The time interval $\Delta t$ can be created just by making the optical path of the probe beam longer than that of the pump beam. After setting a time point $t$, the perturbation of the system, $\varphi(t)$, is detected. The probe beam path is then changed to give a new $\Delta t$ temporal position, and the probe beam detects the corresponding change in the system again. This procedure is repeated until the entire nonequilibrium response profile of the system is measured. In the study of magnetization reversal dynamics, the nonequilibrium state $\varphi(t)$ corresponds to the magnetization switching process excited by magnetic pulses. Typically, a synchronously triggered transient magnetic pulse is propagated past the sample under study, perturbing the magnetization system, and the subsequent evolution of the magnetization configuration is monitored through its interaction with a time-delayed probe beam. The experimental details of the time-resolved magneto-optical Kerr effect technique are described in the next section.

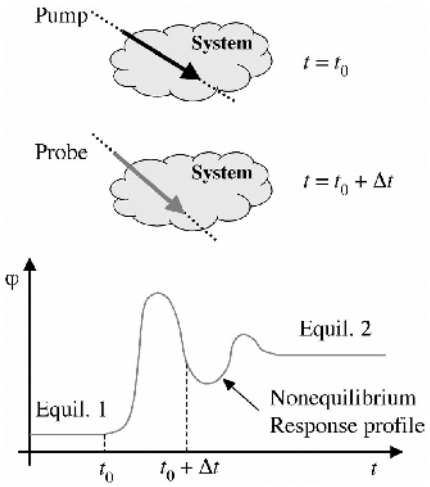


**Fig. 3.2.** Schematic illustration of the "pump-and-probe" technique. At time $t = t_0$, the system is excited out of its equilibrium with the pump pulse. After a short time interval $\Delta t$, the system is probed with the probe pulse. The time delay between the probe and pump beam is then changed to give a new $\Delta t$ temporal position and the signal built-up again. This procedure is repeated until the entire nonequilibrium profile is measured

### 3.2.3 Experimental Apparatus

Optical microscopy using the magneto-optic Kerr effect is a well-established tool for imaging magnetic microstructures [44, 45]. In the present experimental setup, a stroboscopic technique is implemented, adding a time-resolving capability down into the deep picosecond range [13]. Experimental arrangements are based on a scanning Kerr microscope, including ultrafast solid-state laser and optics, a piezo-driven flexure stage for rastering the sample, and electronics controlling the time-delay of probe beam and magnetic pulse generation. A schematic diagram for the entire system is shown in Fig. 3.3, including the optical and electronic layouts. Details of the particular parts of the apparatus are discussed below.

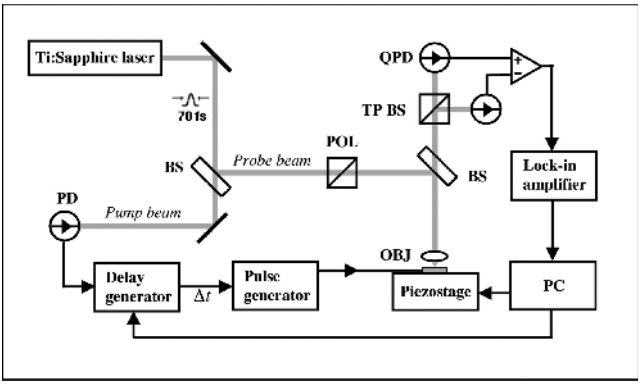


**Fig. 3.3.** A block diagram of the layout of the time-resolved scanning Kerr microscope

#### 3.2.3.1 Optical Setup and Signal Detection

The light source is a mode-locked Ti:Sapphire laser, which provides 70-fs-long pulses of near-infrared light ($\lambda = 800$ nm) with a repetition rate of 82 MHz. During measurement, the pulsed laser beam is split into two beams (i.e., a pump and a probe beam) with a beam splitter (BS). The probe beam passes through a linear polarizer (POL) and is deflected toward the sample and focused onto the sample using an infinity-corrected microscope objective (OBJ), while the pump beam is directed for triggering magnetic pulses (as will be described in more detail below). The optical power of the probe beam is reduced before being brought to a sharp focus on a sample in order to avoid permanent damage to the sample surface. Typically, an average power of 35 μW is focused onto the sample through a microscope objective. The spatial resolution ($d$) is determined by the numerical aperture (N.A.) of the objective lens and wavelength ($\lambda$) of the laser beam, given by the diffraction limited Rayleigh criterion, $d = (0.82\lambda)/\text{N.A.}$ In our experimental setup, a spatial resolution down to 0.9 μm is yielded using the 0.75 N.A. microscope objective and near-infrared light source.

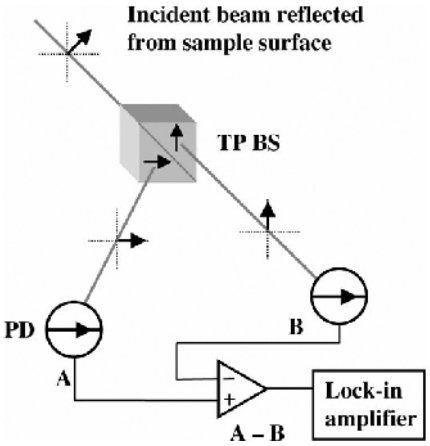


**Fig. 3.4.** Schematic illustration describing differential detection of polarization rotations induced by the magneto-optical Kerr effect. Both outputs of a polarizing beam splitter (at 45° from incident polarization) are used in subtraction. The intensity in each arm rises or falls respectively with rotations of the plane of polarization. The subtracted signal ($A - B$) is only non-zero when a polarization rotation occurs

After the probe beam is reflected from the sample, magnetization measurements are accomplished through the polarization analysis of the reflected light in an optical bridge. A particular detection method using quadrant photodiodes (QPD) has been recently developed to allow for simultaneous detection of all three magnetization components (i.e., vector magnetometry) [23]. This approach is adopted from static Kerr imaging [46–48] and works equally well in time-resolved measurements. The principle of the differential detection method is schematically depicted in Fig. 3.4. The probe beam reflected from the sample surface is split into two orthogonal polarization states by the Thomson polarizing beam splitter (TP BS), which is set at 45° to the incident polarization plane. Consequently, equal intensities are sent to the photodiodes. If there is no polarization rotation in the incident beam, each portion of the split beam will be of equal intensity and differential subtraction of the outputs coming from the two photodiodes will result in a zero signal. A small polarization rotation induced by the magnetization in the sample, however, will be turned into an intensity shift by the Thomson analyzer, in which the intensity in one PD increases while decreasing in the other. This differential detection technique, where each PD signal is used as a reference to the other, has the advantage of common mode rejection of laser noise while doubling the signal [47, 50].

Another important issue in the signal detection is the signal-to-noise ratio, which has always been a problem in Kerr imaging due to the weak magneto-optic Kerr effect (see Sect. 3.2.1.). In static Kerr measurements, wide-field imaging with digital enhancement is generally used, in which the image with magnetization pattern is digitally subtracted from an image of magnetization saturation [51]. This technique removes edge defect and optical system polarization artifacts. In our experimental

setup, signal enhancement is achieved at each pixel of a raster scan using synchronous modulation of the magnetic excitation and lock-in signal detection technique. The modulated magnetic excitation is accomplished by modulating the trigger electronics, which generates magnetic pulses, at a low frequency ($1 \sim 4$ kHz), as described below. The modulation on the magnetization in the sample itself isolates the signal from other artifacts, such as depolarizing effects, in the system.

#### 3.2.3.2 Synchronization and Magnetic Pulse Generation

In stroboscopic imaging, the temporal excitation ("pumping") of the system must be repetitive and triggered synchronously with the probe pulses. This is because interactions of many probe pulses and repetitive excitation events are averaged and represented as a single event. Such a synchronization is achieved as a portion of the laser pulse itself triggers magnetic pulses, which are used to excite the nonequilibrium magnetic state of the sample while another portion of the pulse probes (Fig. 3.2).

In our experimental setup (Fig. 3.3), pump pulses are directed to a fast photodiode (e.g., ThorLabs DET210), which creates and sends clock signals to the variable electronic delay generator (Stanford Research Systems DG535). At this stage, the repetition rate of the pulsed beam is reduced from 82 to 0.8 MHz via pulse picking of the mode-locked laser pulse train. This is required since the maximum trigger rate of the delay generator electronics is limited to 1 MHz. On the other hand, the delay electronics creates the propagation delay on the order of 100 ns. Therefore, an additional time delay between the pump and probe beam is required to achieve temporal synchronization. This can be achieved by delaying the pump beam by an equivalent amount by propagation through a length of coaxial cable until the current pulse is actually synchronized with the laser pulse immediately following the one it was triggered by. After setting a time delay $\Delta t$, the delay generator sends the clock pulses on to the pulse generator.

The electronic delay method is very convenient, particularly when delay ranges of 10 ns or more are needed, but adds jitter of about 50 ps rms. This trigger jitter is the main limiter of temporal resolution in this case. Alternatively, an optical delay line can be used, in which the travel path of the pump beam with respect to the probe beam is computer controlled using mirrors. This technique is inherently jitter-free and is generally beneficial to measurements for faster (low picosecond regime) processes. However, in practice, the delay range usually spans only a few nanoseconds.

The generation of magnetic pulses relies on the current driver, which is based on the avalanche transistor pulser (Model 2000D Pulse Generator, Picosecond Pulse Labs) using the technique of discharging a transmission line. Pulses from this source have 0.5 ns rise times, 1.5 ns fall times, and pulse widths of 10 ns with the amplitude of 50 V. The current pulses are synchronously triggered by Ti:Sapphire fs laser pulses ($\lambda = 800$ nm, 0.8 MHz repetition rate) and are delivered to micro strip lines, which create magnetic field pulses. The inset in Fig. 3.5 shows an image for such strip lines, on or near which magnetic elements are placed. To excite the sample with an out-of-plane magnetic field pulse, samples are situated between lines and for an in-plane pulse, on top of a line. Strip lines are fabricated using lithographic techniques

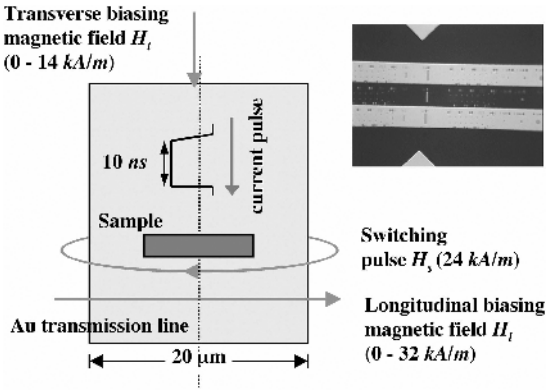


**Fig. 3.5.** Schematic measurement configuration of a 180° dynamic magnetization reversal experiment for microstructure excitation. $H_s$, $H_l$, and $H_t$ indicate the switching field, longitudinal (easy-axis) biasing field, and transverse (hard-axis) biasing field, respectively. In the inset, an image using an optical microscope is given showing magnetic elements on top of or near the gold transmission lines

and have the width of 20 μm and thickness of 300 nm in this case. The strip lines create magnetic pulses as high as 24 kA/m. The temporal shape of field pulses can be measured by a commercially available 2 GHz inductive probe (Tektronix CT-6), or by measuring Faraday rotation in a garnet indicator film [12]. A garnet film allows optical measurement of the current waveforms in a very high bandwidth (over 50 GHz), in addition to providing an absolute time reference for the time-resolved magnetic measurements [23].

### 3.2.3.3 System Operation

Generally, two operation modes are usually employed in TR-SKM experiments. Temporal-resolving mode: One can obtain a majority of the information very efficiently by measuring the dynamic response of the magnetic state of the sample as a function of time. In this mode, the probe beam is focused on a particular place of the sample surface, and then the time delay $\Delta t$ is changed. The Kerr signal is detected after each time step, building up the time-dependent profile for selected magnetization components. This mode is suitable for quick local characterization of the magnetic dynamics (see an example in Fig. 3.6). Temporal resolution is ultimately limited by the laser pulse width, but practically limited by the trigger jitter from the delay electronics, as described above.

Spatiotemporal-resolving mode: After the time-dependent profile of the magnetization is measured, the sample surface can be scanned at a particular fixed time delay in order to obtain two-dimensional images mapping the magnetization configuration (see an example in Fig. 3.7). This is required since the dynamic response of most systems studied can be spatially nonuniform [13, 14]. Using this measurement mode, the sample is placed on a computer-controlled piezo-driven flexure stage providing

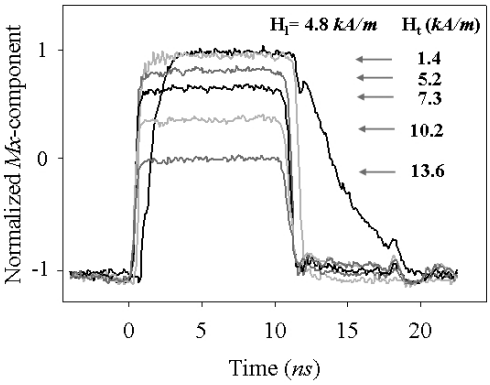


**Fig. 3.6.** Temporal evolution of the easy-axis magnetization component $M_x$ for several values of the transverse biasing field $H_t$ while longitudinal biasing field $H_l$ is being held fixed at 4.8 kA/m. The thick line indicates the magnetization component measured at $H_t = 0$ kA/m. Small peaks found in the back reversal occur due to electrical reflections in the magnetic pulse line

scanning motion at a typical scan rate of 8 pixels/s (which typically corresponds to about 0.3 μm/s). A time record of a few hundred separate sample measurements of the average magnetization was collected for each pixel in the image. Critical in this operation mode is the stability of the piezostage over long time intervals, since the quality of this stage also contributes to the effective spatial resolution of the system. The ThorLab stages used for our data-acquisition were relatively stable, except for slow drifts on the order of 0.5 μm over two or three hours. Such drifts are probably produced by minor fluctuations in the ambient temperature. For high resolution experiments, a positioning feedback stage (such as the Melles Griot feedback stage) would work better, though the Melles Griot feedback has suffered from its own problems such as ringing.

## 3.3 Representative Results in Thin Film Microstructures

In this section, two representative results using TR-SKM are discussed. Experiments are carried out in a microstructure of $Ni_{80}Fe_{20}$ (Permalloy), which is a magnetic alloy used throughout the data storage industry for recording heads. The sample used is a 15-nm-thick polycrystalline $Ni_{80}Fe_{20}$ structure (10 μm × 2 μm) patterned by electron beam lithography. The $Ni_{80}Fe_{20}$ structures are made on a 20-μm-wide and 300-nm-thick gold transmission line that carries a fast current pulse (Fig. 3.5).

### 3.3.1 Picosecond Time-Resolved Magnetization Reversal Dynamics

In the present experiment, a 180° reversal configuration was used (Fig. 3.5). The sample is first saturated in the $x$-direction by an in-plane bias field $H_l$, and then

a switching pulse $H_s$ is applied antiparallel to $H_l$ in order to flip the magnetization. Additionally, an in-plane transverse bias field $H_t$ is applied along the hard axis of the sample to manipulate the switching time and magnetization reversal processes.

Figure 3.6 represents the time dependence of the magnetization component $M_x$ along the easy axis, measured in the center of the structure for different $H_t$, while $H_l$ is kept at 4.8 kA/m. For $H_t = 0$, a definite delay in the magnetic response after the beginning of the pulse is observed. The subsequent dynamics are relatively slow with the magnetization fully reversed after $\sim$ 3.5 ns. Furthermore, the asymmetry between front and back reversal is pronounced, owing to different net switching fields $H_s^{\text{net}}$ driving the switching in the two cases (i.e., 19.2 kA/m for the forward and 4.8 kA/m for the back reversal). Under these field conditions we find $\tau_s = 1.6$ and 7.3 ns for forward and back switching, respectively, defining switching time $\tau_s$ as the interval for 10 to 90% of the total $M_x$ change.

A remarkable difference in the reversal is found by applying a transverse bias field $H_t$. When $H_t$ is applied, the sample responds earlier to the switching pulse. Correspondingly, the rise time rapidly decreases and the magnetization reverses within 1 ns after the beginning of the pulse. The fast switching can be understood as follows: If $H_t$ is applied, the effective $H_c$ is lower than the case where $H_t = 0$. This situation arises because for a finite $H_t$ the equilibrium position of $\boldsymbol{M}$ is away from the easy axis, the position of minimum anisotropy energy. Thus, lower longitudinal Zeeman energy or smaller $H_s$ is required to overcome the energy barrier.

The effect of applying $H_t$ is directly examined through time domain images taken during the reversal. Figure 3.7 shows a sequence of frames illustrating the change of $M_x$. For $H_t = 0$, the reversal is mainly governed by a domain nucleation process. In

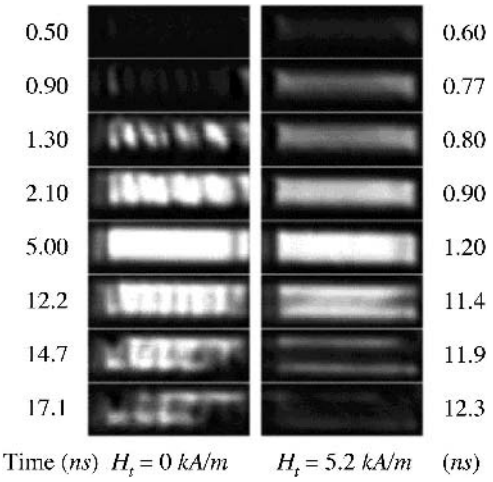


**Fig. 3.7.** Spatial magnetization profiles of $M_x$ component as a function of time (ns) after the magnetic pulse was applied. $H_l = 4.8$ kA/m, while the transverse field are varied $H_t = 0$ and 5.2 kA/m. The field of view of each frame is $12 \times 4$ μm and contains the entire $10 \times 2$ μm sample

the beginning ($t = 0.5$–$0.9$ ns), a stripe-like instability is observed inside the sample. This is followed by expansion of the nucleated domains (1.3 and 2.1 ns), and finally leads to a uniform distribution of fully reversed magnetization, excluding the left and right edge regions (5 ns). These edge regions correspond to free magnetic poles related to the demagnetized areas in a ferromagnet of finite size. On the back reversal, the stripe instability is also pronounced (12.2 ns). From this result, it becomes clear how the switching (Fig. 3.6) evolves spatiotemporally: The finite domain nucleation limits switching time to $\sim 3.5$ ns.

It is this nucleation-dominated reversal process that is manipulated through the application of $H_t$. Applying $H_t = 5.2\,\mathrm{kA/m}$, the 180° domains at the short edges are formed (0.6 ns), but there appears no stripe-like distribution inside. The edge domains expand quickly in the easy-axis direction to form a long, narrow domain parallel to the easy axis (0.77 ns). In the next stage, this elongated domain expands by parallel shifts in the hard direction toward the long edge (0.8 and 0.9 ns) until saturation is reached (1.20 ns). This type of reversal, which is characteristic of domain wall motion, is considerably faster, as revealed in the time dependence of magnetization in Fig. 3.6. The differences in the time domain sequences shown in Fig. 3.7 demonstrate that the formation of nuclei inside the sample is avoided in the presence of $H_t$, and that the nucleation process is replaced by domain wall motion. Switching occurs over longer times when the stripe domains are involved in the reversal process than if pure domain wall motion occurs.

### 3.3.2 Precessional Magnetization Reversal and Domain Wall Oscillation

Another aspect of reversal concerns the time scale and mechanism for the removal of the initial excess Zeeman energy from the system. Coherent oscillations of the magnetization $\boldsymbol{M}$ may be observable after the direction has reversed in cases where the damping is not too strong and where the energy has not propagated into a spin wave manifold, which averages incoherently over the spatial resolution of the measurement (so-called "indirect damping" [52]). In these experiments, this regime is encountered when $\boldsymbol{M}$ is pulsed by $H_s$ in the presence of a high $H_l$ and moderate strength $H_t$. Figure 3.8 shows the time-resolved $M_x$ for different $H_l$ with $H_t = 5.2\,\mathrm{kA/m}$. Two distinct resonance frequencies are found depending on $H_l$. First, small oscillations at $f \sim 2\,\mathrm{GHz}$ are found for $H_l = 8.8$–$10.4\,\mathrm{kA/m}$. It is also apparent that the amplitudes at $H_l = 8.8$ and $9.6\,\mathrm{kA/m}$ rapidly decrease with increasing time. We treat this oscillation as damped ferromagnetic resonance about the new equilibrium direction to infer the saturation magnetization, $M_s$, through $f = \gamma\mu_0(H_t M_s)^{1/2}/(2\pi)$ (derived from the Landau-Liftshitz equation [15]). Using the previously determined value [20], $\gamma = 1.41 \cdot 10^5\ \mathrm{m/s} \cdot$ A yields $\mu_0 M_s = 820\,\mathrm{kA/m}$, close to the bulk value $864\,\mathrm{kA/m}$ for $Ni_{80}Fe_{20}$.

When $H_l$ increases beyond $10.4\,\mathrm{kA/m}$, an oscillation with another frequency occurs, and well-developed oscillations are found at $H_l = 11.2$ and $12\,\mathrm{kA/m}$. This type of oscillation is characteristically a first "spike" followed by a series of smaller oscillations. The spike is an overshoot associated with the application of $H_s$, with over-rotation past what will become the new equilibrium magnetization direction. Some

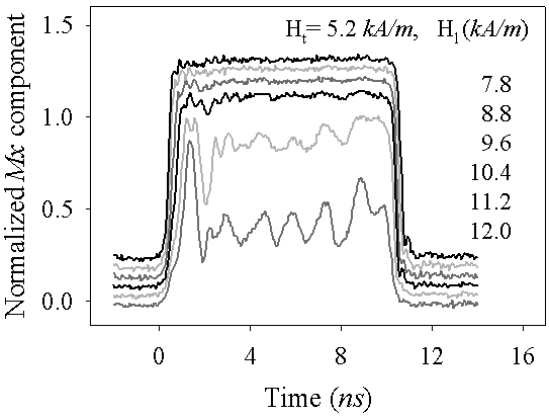


**Fig. 3.8.** Time-resolved $M_x$ component at the center of the element for different $H_l$ with $H_t = 5.2\,\mathrm{kA/m}$. The data are offset vertically in order to compare the oscillation behavior directly

of the excess energy associated with this overshoot subsequently devolves to the new oscillation mode, with a typical frequency of $\sim 0.8\,\mathrm{GHz}$, much lower than that of the previous oscillation. According to the sequence of spatiotemporal magnetization profiles measured over cycles of low frequency oscillation, time domain images at this mode are characterized as a repetitive expansion and withdrawal of elongated domains in the short axis directions, accompanied by a gradual propagation of the domain along the long axis [13]. Therefore, it is concluded that the observed low frequency oscillation originates from domain wall movement and not from the precession of $\boldsymbol{M}$.

## 3.4 Conclusion and Outlook

In summary, the current state of TR-SKM technique is reviewed, showing its significance for metrology in fundamental sciences and industrial applications today. The unique combination of temporal and spatial resolution puts it foremost in elucidating the world of ultrafast phenomena.

A challenging question in the present technique is whether the entire magnetization reversal dynamics studied is perfectly repeatable, since the stroboscopic scanning technique does, by its nature, capture only the repetitive part of the process being imaged. Nonrepetitive instabilities, such as thermal fluctuation of the individual spins, will lead to the averaging of the temporal response. In addition to varying scan rate, number of averages, etc., the most sensitive test for underlying stochastic behavior is found to come from spectrum analysis of the noise on the magneto-optic signal [53]. In the discussed experimental results, however, evidence of additional random behavior has not been observed, and if there is a random component present it is too small to detect.

Desirable for the future TR-SKM studies is the improvement of the spatial resolution, which is limited to 0.9 μm in the present experiments. In order to obtain a higher spatial resolution, an oil immersion objective can be employed. With a 1.3 N.A. oil immersion objective and the same light source, for example, a resolution of 0.65 μm can be obtained. This can again be improved by a factor of two just by converting the near-infrared light into the blue region ($\lambda = 400$ nm), refraining from taking the decrease of the detection efficiency into account. Further improvement of spatial resolution requires the incorporation of a solid immersion lens (SIL) [54] into the stroboscopic technique. Incorporating a solid immersion lens, which uses high index material such as $SrTiO_3$ ($n = 2.4$) or GaP ($n = 3.4$), will improve the spatial resolution considerably down to the order of 100 nm. At some point, however, a crossover to near-field techniques becomes essential if one hopes to extend ultrafast optical imaging to the nanometer scale [55].

*Acknowledgement.* We gratefully acknowledge support from the Natural Sciences and Engineering Research Council of Canada, the Canadian Institute for Advanced Research, and the National Storage Industry Consortium. The samples were produced at the University of Alberta MicroFab, and the experiments performed on equipment donated by Quantum Corporation.

## References

1. S.W. Yuan and H.N. Bertram, J. Appl. Phys. **73**, 5992 (1993).
2. B. Heinrich, Canadian Journal of Physics **78**, 161 (2000).
3. A. Hubert and R. Schäfer, "Magnetic Domains," Springer Verlag, (1999).
4. A.F. Popkov, L.L. Savchenko, N.V. Vorotnikova, S. Tehrani, and J. Shi, Appl. Phys. Lett. **77**, 277 (2000).
5. K.J. Kirk, J.N. Chapman, and C.D.W. Wilkinson, Appl. Phys. Lett. **71**, 539 (1997).
6. J.M. Daughton et al., Thin Solid Films **216**, 162 (1992).
7. W.J. Gallagher et al., J. Appl. Phys. **81**, 3741 (1997).
8. C.H. Back, D. Weller, J. Heidmann, D. Mauri, D. Guarisco, E.L. Garwin, and H.C. Siegmann, Phys. Rev. Lett. **81**, 3251 (1998).
9. C. Stamm, F. Marty, A. Vaterlaus, V. Weich, S. Egger, U. Maier, U. Ramsperger, H. Fuhrmann, and D. Pescia, Science **282**, 449 (1998).
10. M. Hehn, K. Ounadjela, J.-P. Bucher, F. Rousseaux, D. Decanini, B. Bartenlian, and C. Chappert, Science **272**, 1782 (1996).
11. R.P. Cowburn, D.K. Koltsov, A.O. Adeyeye, M.E. Welland, and D.M. Tricker, Phys. Rev. Lett. **83**, 1042 (1999).
12. A.Y. Elezzabi, M.R. Freeman, and M. Johnson, Phys. Rev. Lett. **77**, 3220 (1996).
13. B.C. Choi, G.E. Ballentine, M. Belov, W.K. Hiebert, and M.R. Freeman, Phys. Rev. Lett. **86**, 728 (2001).
14. Y. Acremann, C.H. Back, M. Buess, O. Portmann, A. Vaterlaus, D. Pescia, and H. Melchior, Science **290**, 492 (2000).
15. R.H. Koch, J.G. Deak, D.W. Abraham, P.L. Trouilloud, R.A. Altman, Y. Lu, W.J. Gallagher, R.E. Scheuerlein, K.P. Poche, and S.S.P. Parkin, Phys. Rev. Lett. **81**, 4512 (1998).
16. Y. Martin, H.K. Wickramasinghe, Appl. Phys. Lett. **50**, 1455 (1987).
17. J.N. Chapman, J. Phys. D: Appl. Phys. **17**, 623 (1984).

18. K. Koike and K. Hayakawa, Jpn. J. Appl. Phys. **23**, L187 (1984).
19. J. Unguris, G. Hembree, R.J. Cellota, and D.T. Pierce, J. Microscopy **139**, RP1 (1985).
20. W.K. Hiebert, A. Stankiewicz, and M.R. Freeman, Phys. Rev. Lett. **79**, 1134 (1997).
21. T.M. Crawford, T.J. Silva, C.W. Teplin, and C.T. Rogers, Appl. Phys. Lett. **74**, 3386 (1999).
22. G. Ju, A.V. Nurmikko, R.F.C. Farrow, R.F. Marks, M.J. Carey, and B.A. Gurney, Phys. Rev. Lett. **82**, 3705 (1999).
23. G.E. Ballentine, W.K. Hiebert, A. Stankiewicz, and M.R. Freeman, J. Appl. Phys. **87**, 6830 (2000).
24. W. Dietrich and W.E. Proebster, J. Appl. Phys. **31**, 281S (1960).
25. G.M. Sandler, H.N. Bertram, T.J. Silva, and T.M. Crawford, J. Appl. Phys. **85**, 5080 (1999).
26. T.J. Silva, C.S. Lee, T.M. Crawford, and C.T. Rogers, J. Appl. Phys. **85**, 7849 (1999).
27. S.E. Russek, J.O. Oti, S. Kaka, and E.Y. Chen, J. Appl. Phys. **85**, 4773 (1999).
28. J.F. Dillon, Jr., H. Kamimura, and J.P. Remeika, J. Appl. Phys. **34**, 1240 (1963).
29. M.H. Kryder and F.B. Humphrey, Rev. Sci. Instr. **40**, 829 (1969).
30. P. Kasiraj, D.E. Horne, and J.S. Best, IEEE Trans. Magn. **MAG-23**, 2161 (1987).
31. M.R. Freeman, R.R. Ruf, and R.J. Gambino, IEEE Trans. Magn. **27**, 4840 (1991).
32. A. Stankiewicz, W.K. Hiebert, G.E. Ballentine, K.W. Marsh, and M.R. Freeman, IEEE Trans. Magn. **134**, 1003 (1998).
33. M.R. Freeman, W.K. Hiebert, and A. Stankiewicz, J. Appl. Phys. **83**, 6217 (1998).
34. R.J. Hicken and J. Wu, J. Appl. Phys. **85**, 4580 (1999).
35. J. Reif, J.C. Zink, C.M. Schneider, and J. Kirschner, Phys. Rev. Lett. **67**, 2878 (1991).
36. C.T. Rogers, NSIC (National Storage Industry Consortium) 2000 Symposium, June 26–29 (2000) Monterey, CA, U.S.A. G. Schutz, W. Wagner, W. Wilhelm, P. Kienle, R. Zeller, R. Frahm, and G. Materlik, Phys. Rev. Lett. **58**, 737 (1987).
37. F. Sirotti, R. Bosshard, P. Prieto, G. Panaccione, L. Floreano, A. Jucha, J.D. Bellier, and G. Rossi, J. Appl. Phys. **83**, 1563 (1998).
38. M. Bonfim, G. Ghiringhelli, F. Montaigne, S. Pizzini, N.B. Brookes, F. Petroff, J. Vogel, J. Camarero, and A. Fontaine, Phys. Rev. Lett. **86**, 3646 (2001).
39. S.D. Bader, J. Magn. Magn. Mater. **100**, 440 (1991).
40. S.D. Bader, E.R. Moog, and P. Grünberg, J. Mag. Mag. Mater. **53,** L295 (1986).
41. P.N. Argyres, Phys. Rev. **97**, 334 (1955).
42. D.D. Awschalom, J.-M. Halbout, S. von Molnar, T. Siegrist, and F. Holtzberg, Phys. Rev. Lett. **55**, 1128 (1985).
43. H.J. Williams, F.G. Foster, E.A. Wood, Phys. Rev. **82**, 119 (1951).
44. C. A. Fowler. Jr., E.M. Fryer, Phys. Rev. **86**, 426 (1951).
45. W.W. Clegg, N.A.E. Heyes, E.W. Hill, and C.D. Wright, J. Mag. Mag. Mater **83**, 535 (1990).
46. W.W. Clegg, N.A.E. Heyes, E.W. Hill, and C.D. Wright, J. Mag. Mag. Mater. **95**, 49 (1991).
47. T.J. Silva and A.B. Kos, J. Appl. Phys. **81**, 5015 (1997).
48. B. Petek, P.L. Trouilloud, and B.E. Argyle, IEEE Trans. Magn. **26**, 1328 (1990).
49. P. Kasiraj, R.M. Shelby, J.S. Best, and D.E. Horne, IEEE Trans. Magn. **22**, 837 (1986).
50. P.L. Trouilloud, B. Petek, and B.E. Argyle, IEEE Trans. Magn. **30**, 4494 (1994).
51. M. Ramesh, E. Jedryka, P.E. Wigen, and M. Shone, J. Appl. Phys. **57**, 3701 (1985).
52. M.R. Freeman, R.W. Hunt, and G.M. Steeves, Appl. Phys. Lett. **77**, 717 (2000).
53. J.A.H. Stotz, M.R. Freeman, Rev. Sci. Instrum. **68**, 4468 (1997). E. Betzig, J.K. Trautman, J.S. Weiner, T.D. Harris, and R. Wolfe, Appl. Optics **31**, 4563 (1992).